Applied Physics Letters ARTICLE pubs.aip.org/aip/apl

Experimental observation of negative rotational inertia

Cite as: Appl. Phys. Lett. **123**, 121701 (2023); doi: 10.1063/5.0155865
Submitted: 24 April 2023 · Accepted: 28 August 2023 ·
Published Online: 18 September 2023

View Online Export Citation CrossMark

Shuanglong Liu,[1] Fei Chen,[2,a)] Tian Yang,[1] Robert G. Parker,[2] Pai Wang,[2] and Tianzhi Yang[1,a)]

AFFILIATIONS

[1]School of Mechanical Engineering and Automation, Northeastern University, Shenyang, Liaoning 110819, China
[2]Department of Mechanical Engineering, University of Utah, Salt Lake City, Utah 84112, USA

[a)]Authors to whom correspondence should be addressed: fei.chen@utah.edu and yangtianzhi@me.neu.edu.cn

ABSTRACT

We report an easy-to-make, resonance-based mechanism to realize negative rotational inertia. The device consists of three parts: a heavy inner core, a lightweight outer shell, and rubber connections between the core and shell. We theoretically predict and experimentally observe the negative rotational inertia in the range of 100–230 Hz. The experimental values are obtained via measurements of vibrational response. We further clarify the relation between the bandwidth of negative inertia and the bandgap in a chain consisting of an array of negative-inertia units. The findings reveal a unique property different from conventional systems in classical physics and offer an opportunity for metamaterial designs.

Metamaterials of assembled building blocks can exhibit counterintuitive negative material parameters. In terms of static properties, Lakes reported materials with negative Poisson's ratio[1] in 1987. In terms of wave manipulations, the initial theoretical proposition of optical materials with a negative refractive index was published in 1994.[2] This served as an impetus for researchers to undertake theoretical and computational investigations of metamaterials possessing negative parameters, with the aim of exploring their potential for applications.[3,4] In 2003, a flat optical lens with negative refraction was experimentally verified.[5,6]

In parallel with the flourishing developments of optical materials, negative effective parameters become an emerging topic in acoustic and vibro-elastic metamaterials. Various exotic phenomena were investigated[7–9] after negative density,[10] and a negative modulus[11] was experimentally demonstrated. Negative momentum induced by a positive-momentum excitation was also observed in experiments with a one-dimensional spring-mass system.[12] Negative effective parameters were also investigated in other resonator-based systems, such as one-dimensional chains with mass-in-mass units,[13] metamaterials spring-mass-damper subsystems,[14] elastic architectures consisting of fluid–solid composite inclusions,[15] acoustic double negative metamaterial comprising two coupled membranes,[16] tunable acoustic metamaterials with the multiple degrees of freedom resonating units,[17] and Hilbert-curve-based acoustic metamaterials in the sub-wavelength scale.[18]

Rotational inertia (also known as the moment of inertia, mass moment of inertia, angular mass, or second moment of mass), in general, characterizes materials' ability to resist changes in spinning motion. Hence, they all have positive rotational inertia. In contrast, recent examples with negative rotational inertia[22,23] were theoretically discussed. Although there have been reports that demonstrate the torsional wave band gaps,[24–26] which may indicate the presence of negative rotational inertia, there have yet to be any experimental observations in physical samples. As shown in Fig. 1, experimental evidence of negative rotational inertia remains absent.

In this Letter, we present theoretical analysis and experimental measurements, demonstrating negative rotational inertia in an easy-to-fabricate, two-degree-of-freedom device. It consists of a lightweight outer shell and a heavier inner core. One notable advantage of this system is that its precise characterization is easily achievable because of the simplicity of experimental measurement of the rotational displacements of each part. This allows for an effective comparison of theoretical and experimental results for a range of excitation frequencies. Based on the results, we further analyze a periodic chain with units of negative rotational inertia and reveal the correct relation between the bandgap of the chain and the bandwidth of the unit's negative inertia.

We start with the device shown in Figs. 2(a) and 2(b), which leads to a discrete model for two rotational inertias, I_1 for the shell and I_2 for the core, with a rotational stiffness k_θ between them. The equations of free vibration are

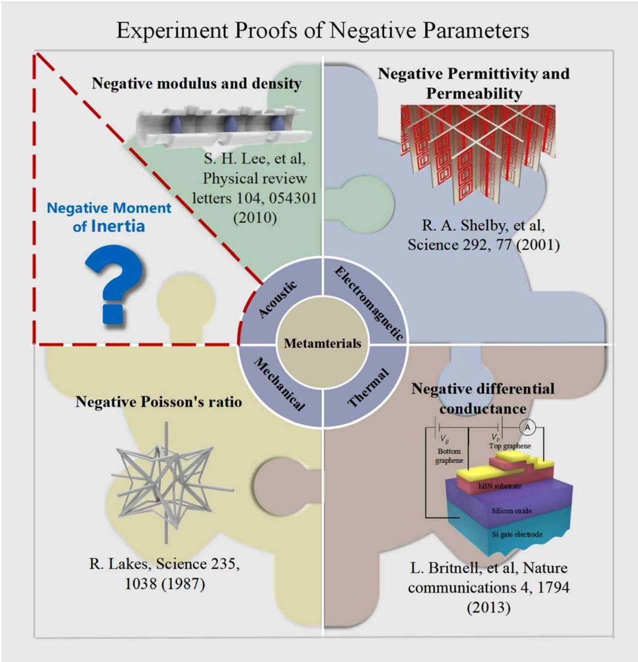

FIG. 1. A concise overview of the history of negative parameters proposed in recent decades, along with some of the representative literature on the topic: Negative modulus and density,[19] Negative Permittivity and Permeability,[20] Negative Poisson's ratio,[1] and Negative differential conductance.[21] The experimental observation of negative effective rotational inertia is currently empty.

$$I_1\ddot{\theta}_1 + k_\theta(\theta_1 - \theta_2) = 0, \tag{1a}$$

$$I_2\ddot{\theta}_2 + k_\theta(\theta_2 - \theta_1) = 0, \tag{1b}$$

where θ_1 and θ_2 are the rotational displacements of the outer shell and the inner core, respectively. This system has two natural frequencies: The first one is zero, which corresponds to the rigid body rotation of the two parts together. The second one is

$$\omega_n = \sqrt{k_\theta \frac{I_1 + I_2}{I_1 I_2}}, \tag{2}$$

which corresponds to the mode of relative rotation between the two parts. In addition, we define the following two "blocked resonance frequencies"[27] by considering one degree of freedom frozen and the other free,

$$\omega_1 = \sqrt{\frac{k_\theta}{I_1}} \quad \text{and} \quad \omega_2 = \sqrt{\frac{k_\theta}{I_2}}. \tag{3}$$

Then, we consider the forced rotational harmonic vibration scenario illustrated in Fig. 2(c). This adds an excitation torque of $\tau(t) = F_0 \cos(\omega t) \cdot r_{11}$ to the right-hand side of Eq. (1a). Here, F_0 denotes the forcing amplitude, ω the driving frequency, and r_{11} the outer radius of the shell. Hence, we can obtain the solution,

$$\theta_1 = \frac{(k_\theta - \omega^2 I_2)\tau}{\omega^4 I_1 I_2 - k_\theta(I_1 + I_2)\omega^2}, \tag{4a}$$

$$\theta_2 = \frac{k_\theta \theta_1}{k_\theta - \omega^2 I_2}. \tag{4b}$$

Next, we treat the entire device as a whole and assume that the inner core is hidden from external observers. Hence, the only observable of this unit's rotation is θ_1. This is similar to the homogenization concept widely used in materials science and metamaterial designs. We now obtain the effective equation of motion,

$$I_{\text{eff}}\ddot{\theta}_1 = \tau, \tag{5}$$

where I_{eff} denotes the effective rotational inertia and θ_1 is the apparent rotational response of the device to an outside observer. From Eqs. (4b) and (5), we can derive

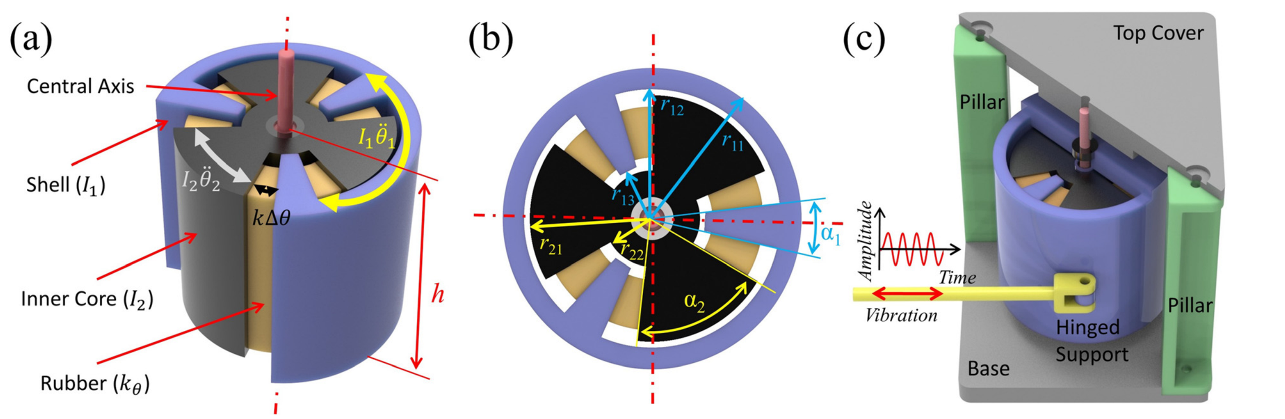

FIG. 2. Schematics of the fabricated device with negative rotational inertia. (a) The overall structure. (b) Top view showing geometric details. The black-colored core with height $h_1 = 0.060$ m has three fins characterized by the angle $\alpha_2 = 75^\circ$ and two radii $r_{21} = 0.038$ m and $r_{22} = 0.015$ m. The blue-colored shell with height $h_2 = 0.057$ m has three internal teeth characterized by the angle $\alpha_1 = 15^\circ$ and three radii $r_{11} = 0.050$ m, $r_{12} = 0.043$ m, and $r_{13} = 0.018$ m. The six pieces of yellow-colored are rubber with height $h_k = 0.057$ m, which is used to bond and secure all three blue fins and all three black fins of both the shell and the core together. (c) Experimental setup for forced vibration tests. The base, top cover, and pillars act as support fixtures.

$$I_{\text{eff}} = \frac{\tau}{-\omega^2\theta_1} = I_1 + \frac{k_\theta I_2}{k_\theta - \omega^2 I_2} = I_1 + \frac{I_2}{1-(\omega/\omega_2)^2}. \tag{6}$$

This shows that we can achieve $I_{\text{eff}} < 0$ as long as we have both

$$\omega > \omega_2 \quad \text{and} \quad I_1 < \frac{I_2}{(\omega/\omega_2)^2 - 1}. \tag{7}$$

Finally, we obtain the following range of driving frequencies associated with the device's negative rotational inertia behavior:

$$\omega_2 < \omega < \sqrt{\frac{I_2+I_1}{I_1}}\omega_2 = \omega_{\text{n}}. \tag{8}$$

Hence, the normalized (dimensionless) frequency bandwidth of the negative rotational inertia phenomenon is

$$\Delta_\omega = \frac{\omega_{\text{n}} - \omega_2}{\omega_2} = \sqrt{\frac{I_2}{I_1}+1} - 1 = \sqrt{\frac{1}{\mu}+1} - 1, \tag{9}$$

where $\mu = I_1/I_2$ is the rotational inertia ratio between the shell and core.

As shown in Fig. 3(a), while both ω_{n} and ω_2 increase with rising rotational inertia ratio $\mu = I_1/I_2$, the dimensional bandwidth $\omega_{\text{n}} - \omega_2$ for the negative rotational inertia effect decreases with increasing μ. At the limit of $\mu \to 0$, it reaches the maximum value of ω_1.

In contrast, the dimensionless bandwidth, Δ_ω, shown in Fig. 3(b), has no upper bound since $\Delta_\omega \to +\infty$ when $\mu \to 0$. In principle, we can obtain any arbitrary large relative bandwidth for the negative rotational inertia phenomenon by minimizing $\mu = I_1/I_2$. The purple vertical dotted lines in Figs. 3(a) and 3(b) illustrate the ratio $\mu = 0.127$ used in the experimental setup, which is described in the next section.

We can also calculate the rotational transmission ratio between the inner core and outer shell,

$$T(\omega) = \left|\frac{\theta_2}{\theta_1}\right| = \left|\frac{k_\theta}{k_\theta - \omega^2 I_2}\right|. \tag{10}$$

At the quasi-static limit of $\omega \to 0$, $T(0^+) = 1$. In addition, $T(\omega) > 1$ for $\omega \in (0, \sqrt{2}\omega_2)$. This is the frequency range in which the rotation is amplified. In contrast, we find $T(\omega) < 1$ for $\omega \in (\sqrt{2}\omega_2, +\infty)$. This is the frequency range in which the rotation is reduced.

We experimentally demonstrate negative rotational inertia under forced vibration conditions. The design is inspired by a gear transmission system. The inner core acts as a three-teeth-spur gear with a larger rotational inertia I_2 than that of the shell I_1. The size of each component and the experimental setup are shown in Fig. 2. The outer shell is made by 3D printing with polylactic acid (PLA) that has density $\rho_1 = 650\,\text{kg/m}^3$. The inner core is made of steel with density $\rho_2 = 7800\,\text{kg/m}^3$. Measurements give their rotational inertia as $I_1 = 2 \times 10^{-4}\,\text{kgm}^2$ and $I_2 = 9.2 \times 10^{-4}\,\text{kgm}^2$. We use six pieces of natural rubber to connect the core and shell. Measurements find the total rotational stiffness as $k_\theta = 340.7\,\text{Nm/rad}$. Importantly, we also make sure that the rotational inertia of rubber pieces are negligible as compared to core and shell. Detailed discussion on measurement and calculation procedures is given in the supplementary material. Cyanoacrylate glues are used to bind the inner core, rubber pieces, and shell together, as shown in Figs. 2(a) and 2(b). The inner core and outer shell are free to rotate around the low-friction central axle made of stainless steel.

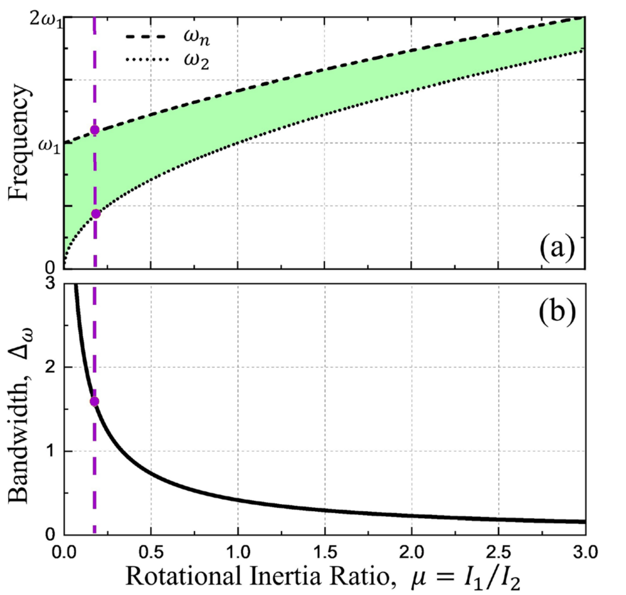

FIG. 3. Theoretical prediction on the bandwidth of negative rotational inertia for varying inertia ratio $\mu = I_1/I_2$. (a) The green-shaded region represents the dimensional bandwidth. (b) The black solid line represents the dimensionless bandwidth. The vertical purple-dotted lines illustrate the dimensional and dimensionless bandwidths corresponding to $\mu = 0.217$, which is measured from the fabricated experimental sample.

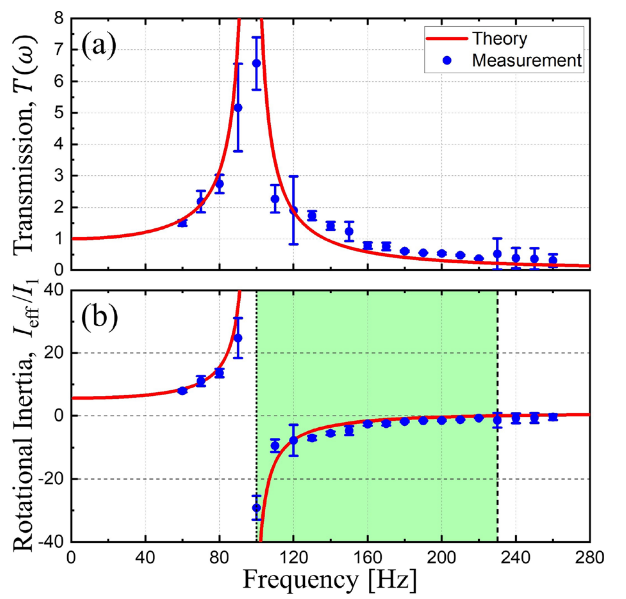

FIG. 4. Comparison of the measured data (blue squares) and theoretical predictions (red lines). The error bars indicate the maximum and minimum values from five repeated measurements. (a) The transmission coefficient T is strongly frequency-dependent. (b) The normalized effective rotational inertia I_{eff}/I_1 is also strongly frequency-dependent. In the range from 100 to 230 Hz (green-shaded region), we achieve a negative rotational inertia $I_{\text{eff}} < 0$.

As shown in Fig. 2(c), to excite a small-angle rotational oscillation, a shaker (SA-JZ002) is connected with a hinge along the tangential direction of the outer cylindrical shell. Two miniaturized lightweight accelerometers (CA-YD-103 with diameter = 14 mm, height = 19 mm, and weight = 13 g) are glued to the inner core and outer shell. Tests are performed in the range of 60–270 Hz with a 10 Hz increment. Five repeated measurements are conducted for each frequency on the same experimental setup.

Equations (6) and (8) predict that the value of I_{eff} becomes negative when the excitation frequency ω is between 97 and 227 Hz. For a clear comparison, experimental measurements of the effective rotational inertia are plotted as blue squares with error bars in Fig. 4, where the theoretical values are plotted as red lines. On the one hand, the experimental data in Fig. 4(a) show the resonant behavior near $\omega_2 = 97$ Hz. On the other hand, Fig. 4(b) shows that the value of I_{eff} diverges at the resonant frequency. Furthermore, the experimental measurements confirm that the device has negative rotational inertia for the excitation frequencies from $\omega = 100$ Hz to $\omega = 230$ Hz.

Next, we investigate the effect of units of negative rotational inertia in a periodic chain and explore the potential for such a metamaterial in manipulating the torsional wave propagation. This adds another system parameter of rotational stiffness, K_θ, which connects

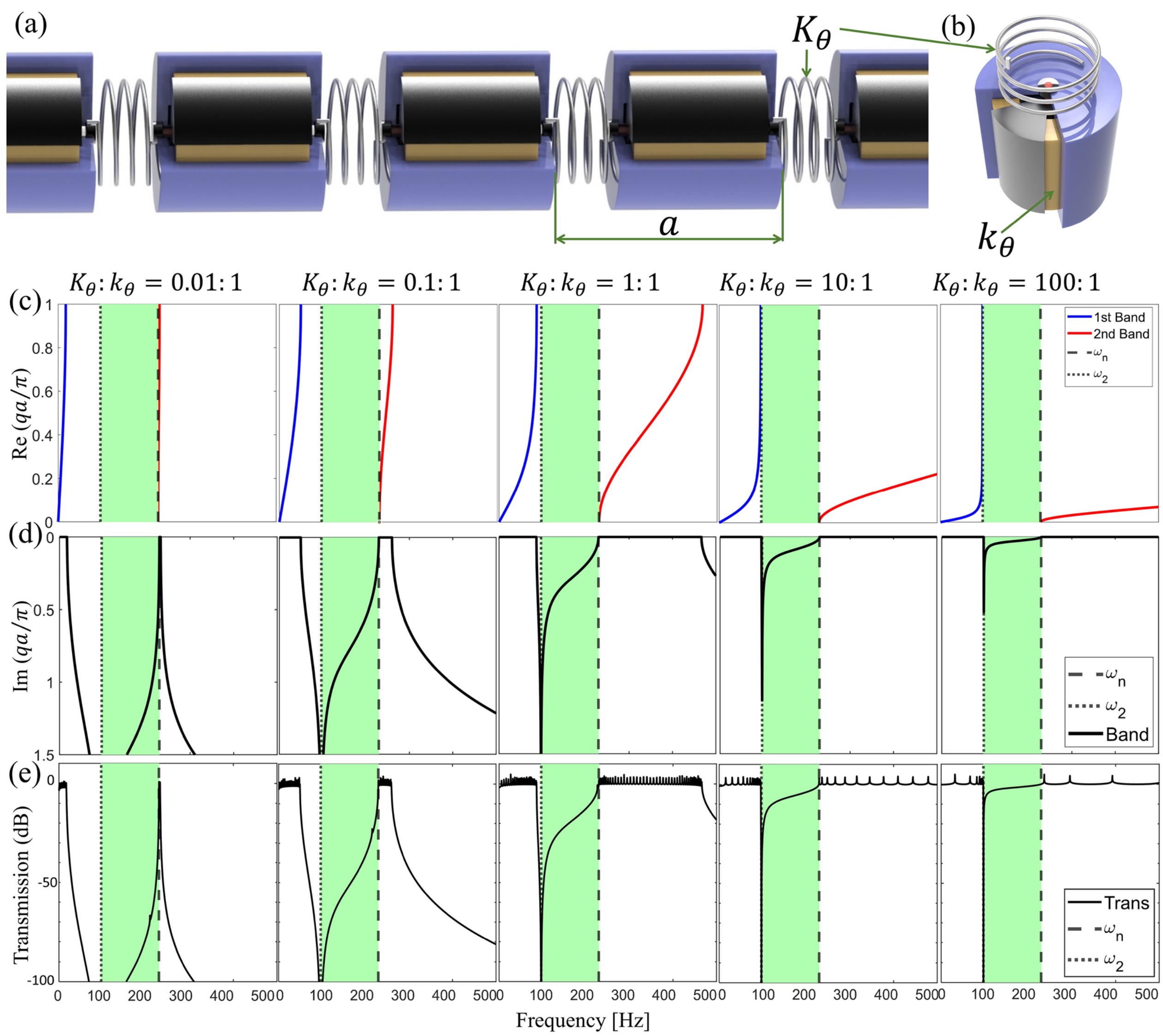

FIG. 5. (a) A periodic chain of units with negative rotational inertia. All the units are arranged along the same axis, and each unit is connected to its neighbor by a torsional spring K_θ. (b) A unit cell of the chain. The dispersion relations of torsional waves on the chain are plotted by varying the stiffness ratio $K_\theta/k_\theta = 10^{-2}, 10^{-1}, 10^{0}, 10^{1}$, and$10^{2}$. (c) and (d) The real and imaginary parts of the dispersion, respectively. The vertical axes represent the dimensionless angular wave number q, which is related to the wavelength λ by $q = 2\pi/\lambda$. The green-shaded regions indicate the frequency bandwidth in which the units exhibit negative rotational inertia, with the upper bound ($\omega_{\mathrm{U}} = \omega_{\mathrm{n}}$) marked by the vertical dashed lines and the lower bound ($\omega_{\mathrm{L}} = \omega_2$) marked by the vertical dotted line. (e) The vibration transmission of a finite chain, which has 50 units.

the outer shells between all pairs of units, as illustrated in Figs. 5(a) and 5(b). There are two degrees of freedom in each unit, so we can get a two-band dispersion for the chain. By varying the stiffness ratio of K_θ/k_θ, we plot the real part of the dispersion curves for torsional waves propagating in the chain, cyan-colored first band and magenta-colored second band, in Fig. 5(c). In these same plots, we also highlight the frequency bandwidth of the negative rotational inertia phenomenon as the green-shaded region. Equation (8) dictates that this bandwidth is between the upper- and lower-frequency bounds of

$$\omega_{\mathrm{U}} = \omega_{\mathrm{n}} = \sqrt{k_\theta \frac{I_1 + I_2}{I_1 I_2}}, \tag{11a}$$

$$\omega_{\mathrm{L}} = \omega_2 = \sqrt{\frac{k_\theta}{I_2}}, \tag{11b}$$

which are plotted as the dashed and dotted lines, respectively, in Figs. 3(a), 4(b), and 5(c)–5(e). This bandwidth does not change throughout all cases since it is strictly a unit-cell property, and it does not depend on K_θ.

In contrast, by following similar procedures adopted in previous theoretical analyses,[28,29] we can obtain the frequency limits of the bandgap of the periodic chain as

$$\omega_{\mathrm{GapU}} = \sqrt{k_\theta \frac{I_1 + I_2}{I_1 I_2}} = \omega_{\mathrm{n}} = \omega_{\mathrm{U}}, \tag{12a}$$

$$\omega_{\mathrm{GapL}} = \sqrt{\chi - \sqrt{\chi^2 - 4\omega_2^2 \Omega_1^2}}, \tag{12b}$$

where

$$\chi = \frac{k_\theta}{2I_1} + \frac{k_\theta}{2I_2} + \frac{2K_\theta}{I_1} = \frac{\omega_1^2}{2} + \frac{\omega_2^2}{2} + 2\Omega_1^2 \tag{13}$$

and $\Omega_1 = \sqrt{K_\theta/I_1}$. While the upper edge of the bandgap coincides with the upper bound of negative rotational inertia (i.e., $\omega_{\mathrm{GapU}} = \omega_{\mathrm{U}}$), the lower edge of the bandgap is different from the lower bound of negative rotational inertia (i.e., $\omega_{\mathrm{GapL}} \neq \omega_{\mathrm{L}}$). Hence, contrary to the pervasive misconception,[12,30–34] the bandgap frequency range is not necessarily equivalent to negative-inertia bandwidth. As shown in the first two columns of Fig. 5(c), the bandgap can be much wider than the negative-inertia bandwidth when $K_\theta < k_\theta$. In fact, asymptotic analyses of Eqs. (12b) and (13) show that we can have $\omega_{\mathrm{GapL}} \to \omega_{\mathrm{L}}$ at the limit of $K_\theta \gg k_\theta$.

To complete the numerical discussion, we also present the imaginary part of the dispersion relations in Fig. 5(d). In spite of the varying stiffness ratio of K_θ/k_θ and the varying gap sizes, the imaginary dispersion curves in Fig. 5(d) always display the valleys of strongest attenuation that are precisely at the lower bound for negative rotational inertia: $\omega_{\mathrm{L}} = \omega_2$. Furthermore, we study the vibration transmission of a finite chain with 50 unit cells. We use an excitation torque of $\tau(t) = F_0 \cos(\omega t) \cdot r_{11}$ on the first unit's shell and then obtain the transmission in dB as

$$\mathrm{Transmission}(\omega) = 20 \log_{10} \left| \frac{\theta_{50}^{I_1}}{\theta_1^{I_1}} \right|, \tag{14}$$

where $\theta_1^{I_1}$ and $\theta_{50}^{I_1}$ are response rotations of the shell parts of the first and last units, respectively. As shown in Fig. 5(e), the finite-chain transmission agrees with the imaginary part of the dispersion in Fig. 5(d). Further details regarding finite chains consisting of different numbers of units can be found in the supplementary material.

In summary, we fabricate a cylindrical device of the size 0.1 m in diameter and 0.06 m in height and experimentally measure its frequency-dependent rotational inertia. The design consists of a heavy inner core, a lightweight outer shell, and rubber connections between the core and shell. In the frequency range from 100 to 230 Hz, our experimental observations show that this device exhibits negative rotational inertia. Through theoretical analysis, we also find that the dimensionless operating bandwidth can be arbitrarily wide for the phenomenon of negative rotational inertia. In addition, we numerically analyze the torsional wave propagation on a periodic chain consisting of such units of negative rotational inertia. By presenting both real and imaginary parts of the dispersion relations, we further clarify the relationship between the torsional wave bandgap in the chain and the bandwidth of the negative rotational inertia phenomenon. In addition, we study the vibration transmission of finite systems. This study extends the classical concept of rotational inertia and demonstrates that it can be positive or negative in different frequency ranges. The findings may pave the way to explore physical phenomena of rotational vibrations and torsional waves in solids.

See the supplementary material for photos and data of experimental testing and parametric measurements of the device's each component.

P.W. acknowledges the support from the startup research funds of the Department of Mechanical Engineering at the University of Utah. The support and resources from the Center for High-Performance Computing at the University of Utah are gratefully acknowledged. T.Z.Y. acknowledges that this work was supported by the National Science Foundation of China (Grant Nos. 12232014 and 12072221), Central Universities (Grant No. 2013017), and the Ten Thousand Talents Program.

AUTHOR DECLARATIONS

Conflict of Interest

The authors have no conflicts to disclose.

Author Contributions

Shuanglong Liu: Conceptualization (equal); Data curation (equal); Formal analysis (equal); Methodology (equal); Project administration (equal); Validation (equal); Visualization (lead); Writing – original draft (equal). **Fei Chen:** Data curation (equal); Formal analysis (equal); Methodology (equal); Supervision (equal); Validation (equal); Writing – original draft (equal). **Tian Yang:** Data curation (equal); Validation (equal). **Robert G. Parker:** Data curation (equal); Methodology (equal); Validation (equal). **Pai Wang:** Methodology (equal); Supervision (equal); Validation (lead); Writing – review & editing (lead). **Tianzhi Yang:** Conceptualization (equal); Formal analysis (equal); Project administration (equal); Resources (equal); Supervision (equal); Validation (equal); Writing – review & editing (equal).

DATA AVAILABILITY

The data that support the findings of this study are available from the corresponding authors upon reasonable request.

REFERENCES

[1]R. Lakes, "Foam structures with a negative Poisson's ratio," Science **235**, 1038–1040 (1987).

[2]N. Nicorovici, R. C. McPhedran, and G. W. Milton, "Optical and dielectric properties of partially resonant composites," Phys. Rev. B **49**, 8479 (1994).

[3]J. Li and C. T. Chan, "Double-negative acoustic metamaterial," Phys. Rev. E **70**, 055602 (2004).

[4]C. T. Chan, J. Li, and K. H. Fung, "On extending the concept of double negativity to acoustic waves," J. Zhejiang Univ.-Sci. A **7**, 24–28 (2006).

[5]P. V. Parimi, W. T. Lu, P. Vodo, and S. Sridhar, "Imaging by flat lens using negative refraction," Nature **426**, 404–404 (2003).

[6]D. R. Smith, J. B. Pendry, and M. C. Wiltshire, "Metamaterials and negative refractive index," Science **305**, 788–792 (2004).

[7]M.-H. Lu, C. Zhang, L. Feng, J. Zhao, Y.-F. Chen, Y.-W. Mao, J. Zi, Y.-Y. Zhu, S.-N. Zhu, and N.-B. Ming, "Negative birefraction of acoustic waves in a sonic crystal," Nat. Mater. **6**, 744–748 (2007).

[8]J. Christensen, A. I. Fernandez-Dominguez, F. de Leon-Perez, L. Martin-Moreno, and F. Garcia-Vidal, "Collimation of sound assisted by acoustic surface waves," Nat. Phys. **3**, 851–852 (2007).

[9]Y. Ding, Z. Liu, C. Qiu, and J. Shi, "Metamaterial with simultaneously negative bulk modulus and mass density," Phys. Rev. Lett. **99**, 093904 (2007).

[10]Z. Liu, X. Zhang, Y. Mao, Y. Zhu, Z. Yang, C. T. Chan, and P. Sheng, "Locally resonant sonic materials," Science **289**, 1734–1736 (2000).

[11]N. Fang, D. Xi, J. Xu, M. Ambati, W. Srituravanich, C. Sun, and X. Zhang, "Ultrasonic metamaterials with negative modulus," Nat. Mater. **5**, 452–456 (2006).

[12]S. Yao, X. Zhou, and G. Hu, "Experimental study on negative effective mass in a 1d mass–spring system," New J. Phys. **10**, 043020 (2008).

[13]H. Huang, C. Sun, and G. Huang, "On the negative effective mass density in acoustic metamaterials," Int. J. Eng. Sci. **47**, 610–617 (2009).

[14]H. Sun, X. Du, and P. F. Pai, "Theory of metamaterial beams for broadband vibration absorption," J. Intell. Mater. Syst. Struct. **21**, 1085–1101 (2010).

[15]Y. Wu, Y. Lai, and Z.-Q. Zhang, "Elastic metamaterials with simultaneously negative effective shear modulus and mass density," Phys. Rev. Lett. **107**, 105506 (2011).

[16]M. Yang, G. Ma, Z. Yang, and P. Sheng, "Coupled membranes with doubly negative mass density and bulk modulus," Phys. Rev. Lett. **110**, 134301 (2013).

[17]P. Wang, F. Casadei, S. Shan, J. C. Weaver, and K. Bertoldi, "Harnessing buckling to design tunable locally resonant acoustic metamaterials," Phys. Rev. Lett. **113**, 014301 (2014).

[18]X. Man, Z. Luo, J. Liu, and B. Xia, "Hilbert fractal acoustic metamaterials with negative mass density and bulk modulus on subwavelength scale," Mater. Des. **180**, 107911 (2019).

[19]S. H. Lee, C. M. Park, Y. M. Seo, Z. G. Wang, and C. K. Kim, "Composite acoustic medium with simultaneously negative density and modulus," Phys. Rev. Lett. **104**, 054301 (2010).

[20]R. A. Shelby, D. R. Smith, and S. Schultz, "Experimental verification of a negative index of refraction," Science **292**, 77–79 (2001).

[21]L. Britnell, R. Gorbachev, A. Geim, L. Ponomarenko, A. Mishchenko, M. Greenaway, T. Fromhold, K. Novoselov, and L. Eaves, "Resonant tunnelling and negative differential conductance in graphene transistors," Nat. Commun. **4**, 1794 (2013).

[22]L. Yang and L. Wang, "An ultrawide-zero-frequency bandgap metamaterial with negative moment of inertia and stiffness," New J. Phys. **23**, 043003 (2021).

[23]J. Lončar, B. Igrec, and D. Babić, "Negative-inertia converters: Devices manifesting negative mass and negative moment of inertia," Symmetry **14**, 529 (2022).

[24]G. Ma, C. Fu, G. Wang, P. Del Hougne, J. Christensen, Y. Lai, and P. Sheng, "Polarization bandgaps and fluid-like elasticity in fully solid elastic metamaterials," Nat. Commun. **7**, 13536 (2016).

[25]K. Wang, J. Zhou, C. Cai, D. Xu, S. Xia, and G. Wen, "Bidirectional deep-subwavelength band gap induced by negative stiffness," J. Sound Vib. **515**, 116474 (2021).

[26]Z. Dong and P. Sheng, "Inertial-amplified mechanical resonators for the mitigation of ultralow-frequency vibrations," Phys. Rev. Appl. **18**, 014027 (2022).

[27]A. S. Phani, "Dissipation driven degeneracies," Appl. Phys. Lett. **121**, 231701 (2022).

[28]H. Al Ba'ba'a, M. Nouh, and T. Singh, "Formation of local resonance band gaps in finite acoustic metamaterials: A closed-form transfer function model," J. Sound Vib. **410**, 429–446 (2017).

[29]F. Jamil, F. Chen, B. Deng, R. G. Parker, and P. Wang, "Inerter-based elastic metamaterials for band gap at extremely low frequency," Extreme Mech. Lett. **56**, 101847 (2022).

[30]X.-N. Liu, G.-K. Hu, G.-L. Huang, and C.-T. Sun, "An elastic metamaterial with simultaneously negative mass density and bulk modulus," Appl. Phys. Lett. **98**, 251907 (2011).

[31]S. H. Lee, C. M. Park, Y. M. Seo, Z. G. Wang, and C. K. Kim, "Acoustic metamaterial with negative density," Phys. Lett. A **373**, 4464–4469 (2009).

[32]G. Huang and C. Sun, "Band gaps in a multiresonator acoustic metamaterial," J. Vib. Acoust. **132**(3), 031003 (2010).

[33]Q. Lin, J. Zhou, K. Wang, D. Xu, G. Wen, Q. Wang, and C. Cai, "Low-frequency locally resonant band gap of the two-dimensional quasi-zero-stiffness metamaterials," Int. J. Mech. Sci. **222**, 107230 (2022).

[34]Y. Chen, G. Huang, and C. Sun, "Band gap control in an active elastic metamaterial with negative capacitance piezoelectric shunting," J. Vib. Acoust. **136**(6), 061008 (2014).

Supplementary Materials

Experimental Observation of Negative Rotational Inertia

Shuanglong Liu,[1] Fei Chen,[2,*] Tian Yang,[1] Robert G. Parker,[2]

Pai Wang,[2] and Tianzhi Yang[1,†]

[1]*School of Mechanical Engineering and Automation,*

Northeastern University, Shenyang, Liaoning 110819, China

[2]*Department of Mechanical Engineering,*

University of Utah, Salt Lake City, UT 84112, USA

• Experimental Testing:

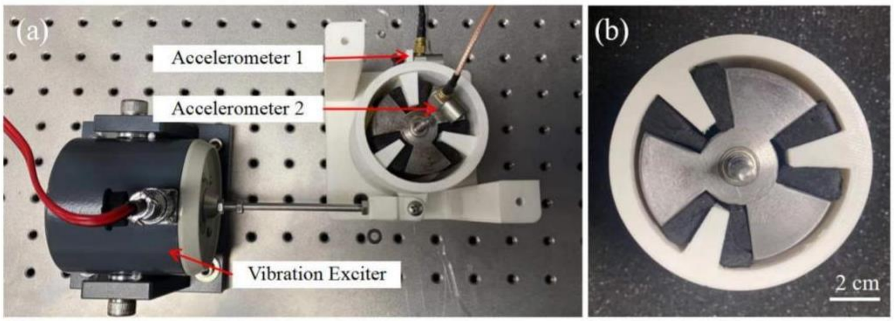

FIG. S1 Schematic diagram of the experimental principle and structure of the experimental model.

We fabricate the device of the inner core (I_2) and the outer shell (I_1), and then conduct measurements under an external excitation $f(t) = F_0\cos(\omega t)$. The angular accelerations $\ddot{\theta}_2 = A_2\cos(\omega t)$ of the inner core and $\ddot{\theta}_1 = A_1\cos(\omega t)$ of the outer shell are obtained by accelerometer 1 and accelerometer 2, respectively. Based on Eqs. (6) and (10), the Figure 4 can be obtained with experimental data. The measurements are tested in the range of 60 *Hz* - 270 *Hz* with a 10 Hz increment, data for each measurement as shown in Table. S1.

Table. S1 Measured data for Shell (A_1) and Core (A_2)

Frequency (Hz)	$\|A_2\|$(g)	$\|A_1\|$ (g)	$\|A_2\|$ (g)	$\|A_1\|$ (g)	$\|A_2\|$ (g)	$\|A_1\|$ (g)
60	3.1892	4.5456	3.2724	4.3276	4.1789	5.2656
70	1.8511	1.7244	2.8858	3.1018	3.0683	2.4167
80	2.8923	2.3756	6.24536	4.50187	6.14432	4.09183
90	4.76845	1.98694	14.76137	4.41052	2.34567	1.1762
100	8.04543	2.36596	8.09004	2.86549	4.64167	1.28022
110	12.63399	9.328	2.79719	2.48988	6.34248	6.87789
120	3.68391	2.34832	2.02406	3.38831	3.20551	4.6785
130	6.54021	7.60588	6.21987	7.78654	5.39636	5.73362
140	2.37787	3.58523	3.19669	4.72444	2.60029	3.35279
150	4.32813	8.77499	4.31335	5.49092	4.16466	7.33913
160	3.09596	6.91868	1.91587	5.23503	2.91358	8.15
170	3.38103	8.53593	1.9004	6.12129	1.92649	4.54758
180	1.74465	5.5361	2.84761	9.50055	2.59868	8.95496
190	2.11598	7.66448	3.32058	12.15665	2.60443	9.36319
200	1.90168	7.37483	2.78655	11.04925	1.97772	6.92854
210	1.37441	5.96156	2.60571	10.37513	2.16545	9.29019
220	1.8376	10.28222	1.31849	7.22952	1.03637	5.49195
230	0.59323	5.1125	0.93116	8.00831	8.18594	15.06809
240	0.9971	10.30642	1.39496	14.12741	3.44694	9.14561
250	1.21588	10.03212	0.58029	11.37817	5.14931	13.92143
260	1.30164	13.09309	1.42821	15.16731	3.6952	13.77325

• Parametric Measurements

The rubber is placed according to the experimental conditions, one side is horizontal and the other side is rotated under pressure, the force F_k perpendicular to the horizontal is measured at different angles at a distance L from the centre of rotation of the system, and an expression is obtained for the relationship between the moment M_k applied to the rubber and the angle θ_0 of compression.

$$M_k = F_k L \sin(\theta_k - \theta_0) \tag{S1}$$

where θ_k is the magnitude of the angle when the force on the system is zero.

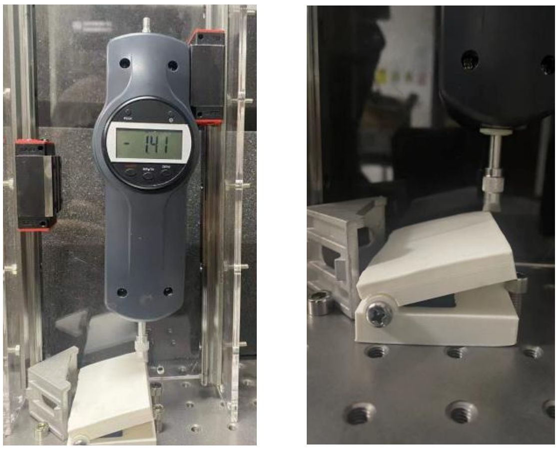

FIG S2. Measuring the rotational stiffness of rubber.

Table S2. Torque applied to each rubber at different angles.

Angle (°)	Rubber 1 (Nm)		Rubber 2 (Nm)		Rubber 3 (Nm)		Rubber 4 (Nm)		Rubber 5 (Nm)		Rubber 6 (Nm)	
1	1	0.96	1.02	1.05	1.02	0.96	0.93	0.92	0.96	0.94	0.96	1.01
2	1.78	1.83	2.03	2.13	2.12	2.04	1.89	1.96	1.9	1.95	1.9	1.95
3	2.99	2.92	3.17	3.07	3.02	2.78	2.73	2.92	3.12	3.13	3	3.06

Table S3. Parameters of Each Component of the Device.

No.	E	h_r (m)	R_1 (m)	R_2 (m)	k_θ (Nm/rad)
1.	4.25Mpa	0.05	0.015	0.0385	55.66
2.		0.053	0.015	0.0375	59.61
3.		0.05	0.015	0.0365	56.45
4.		0.05	0.015	0.037	54.09
5.		0.055	0.015	0.036	58.04
6.		0.049	0.015	0.037	56.85

- **Estimates of rotational inertia of rubber bars.**

FIG S3. The mass of one piece of rubber.

$$I_{ring} = \frac{1}{2} m_{ring} (R_2^2 - R_1^2) \tag{S2a}$$

$$I_{r\max} = \frac{1}{2} n m_r (R_{2\max}^2 - R_{1\min}^2) \tag{S2b}$$

The measured mass of one piece of rubber $m_r = 0.3 \times 10^{-3}$ kg. The maximum rotational inertia of the fan ring rubber $I_{r\_max} = 1.04 \times 10^{-6}$ kgm^2 of the system can be found. Therefore, the rotational inertia of the rubber is very small and is ignored in this letter. The R_1 and R_2 values are based on the Table S3.

- **Measurement of rotational moment of inertia by the constant torque method.**

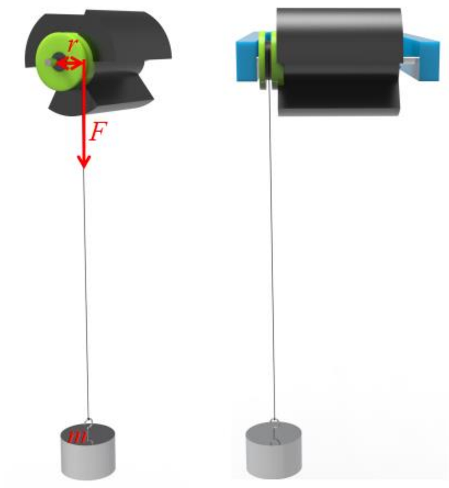

FIG S4. Constant moment method for measuring rotational moment of inertia.

A weight $s = 0.5$ is dropped from rest and the time t of fall is recorded. Friction, the mass of the rope is not accounted for; the rotational inertia of the runner is measured in advance to be $3 \times 10^{-6}\ kg \cdot m^2$. A system with a total rotational inertia I receives a tangential force F from a weight of mass m. The radius of the runner at the winding is r, and the angular acceleration of the weight can be found $\beta = \alpha / r$.Find the instantaneous moment applied to the system $M = I\beta$. The relationship between the fall time t of the weight and the rotational inertia I is obtained.

$$m = \frac{2sI}{gr^2} \cdot \frac{1}{t^2} . \tag{S2}$$

where g is the acceleration of gravity.

Table S4. Experimental results of the measurement I_1 and I_2.

m(kg)	$\bar{t}$ (s)	I (kg.m^2)	Result (kg.m^2)
0.01	3.20	9.21e-4	I_2≈9.2e-4
0.02	2.26	9.19e-4	
0.01	1.5	2.03e-4	I_1≈2e-4
0.02	1.06	2.02e-4	

- **The Vibration Transmission of Finite Chains**

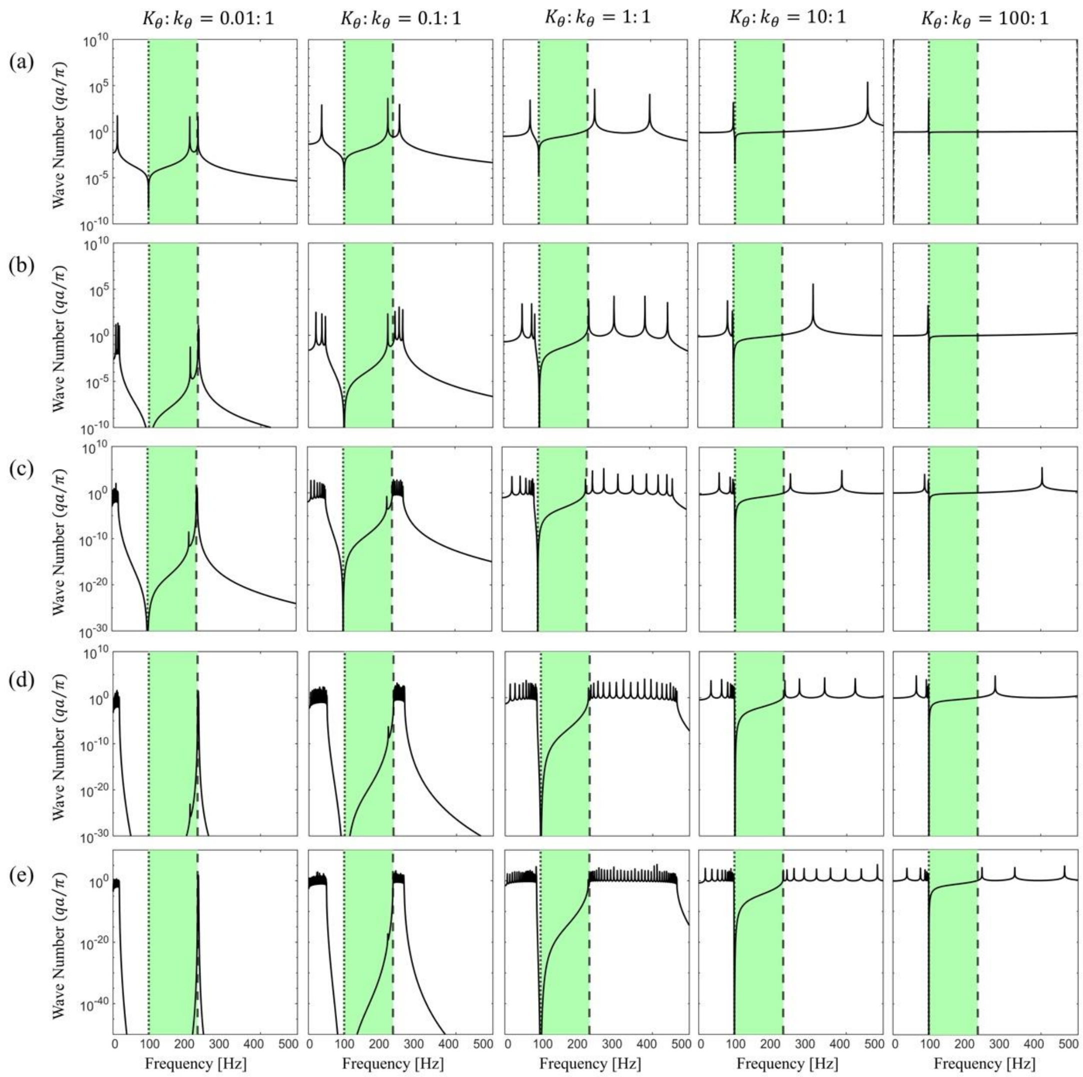

FIG S4. The vibration transmission of periodic chain of units with negative rotational inertia. In addition to results shown in Fig. 5 of the main text, here we present the results of chains with (a) 3, (b) 5, (c) 10, (d) 20, and (e) 40 units. Each chain is investigated with varying the stiffness ratios. The dash lines are ω_n; the dot lines are ω_2, and the solid black lines are the transmission between the last of first unit of the chain.